

Geophysical Research Letters®



RESEARCH LETTER

10.1029/2023GL103809

Key Points:

- Hunga eruption generated extreme horizontal wind perturbations at 80–100 km of altitude over South America
- The signal was detected almost simultaneously by three multistatic meteor radar systems spanning more than 3,000 km
- The perturbation had a period of ~2 hr, a horizontal phase velocity of ~200 m/s, and a horizontal wavelength of ~1,440 km

Correspondence to:






F. L. Poblet,
poblet@iap-kborn.de

Citation:

Poblet, F. L., Chau, J. L., Conte, J. F., Vierinen, J., Suclupe, J., Liu, A., & Rodriguez, R. R. (2023). Extreme horizontal wind perturbations in the mesosphere and lower thermosphere over South America associated with the 2022 Hunga eruption. *Geophysical Research Letters*, 50, e2023GL103809. <https://doi.org/10.1029/2023GL103809>

Received 22 MAR 2023
Accepted 30 MAY 2023

Extreme Horizontal Wind Perturbations in the Mesosphere and Lower Thermosphere Over South America Associated With the 2022 Hunga Eruption

Facundo L. Poblet¹ , Jorge L. Chau¹ , J. Federico Conte¹ , Juha Vierinen² , Jose Suclupe¹, Alan Liu³ , and Rodolfo R. Rodriguez⁴

¹Leibniz Institute of Atmospheric Physics at the University of Rostock, Kühlungsborn, Germany, ²University of Tromsø, Tromsø, Norway, ³Embry-Riddle Aeronautical University, Daytona Beach, FL, USA, ⁴Universidad de Piura, Piura, Peru

Abstract On 15 January 2022, the Hunga volcano produced a massive explosion that generated perturbations in the entire atmosphere. Nonetheless, signatures in the mesosphere and lower thermosphere (MLT) have been challenging to identify. We report MLT horizontal wind perturbations using three multistatic specular meteor radars on the west side of South America (spanning more than 3,000 km). The most notorious signal is an exceptional solitary wave with a large vertical wavelength observed around 18 UT at all three sites, with an amplitude of ~50 m/s mainly in the westward direction. Using a customized analysis, the wave is characterized as traveling at ~200 m/s, with a period of ~2 hr and a horizontal wavelength of ~1,440 km in the longitudinal direction, away from the source. The perturbation is consistent with an L_1 Lamb wave mode. The signal's timing coincides with the arrival time of the tsunami triggered by the eruption.

Plain Language Summary The eruption of the Hunga volcano in January 2022 had a widespread impact on the atmosphere, affecting various layers. We describe a perturbation in horizontal winds caused by the event, which was observed over the west coast of South America by three different meteor radar systems separated by more than 3,000 km between them. The perturbation behaved similarly in the altitude range of 80–100 km, and the wave parameters observed were consistent with high-order Lamb wave solutions from simulations carried out using the Whole Atmosphere Community Climate Model with thermosphere/ionosphere extension. This finding complements other studies that have explored the impacts of the eruption on different atmospheric levels. Overall, this study provides valuable insights into the complex and far-reaching effects of volcanic eruptions on the atmosphere.

1. Introduction

The 15 January 2022 eruption of Hunga volcano, Tonga (Global Volcanism Program, 2022), which began around 4:00 UT, ejected an immense amount of energy into the atmosphere, as well as volcanic tephra and gases into the stratosphere. The eruption released approximately the equivalent of 61 Mt, which is larger than the Tsar Bomba, and the famous 1980 eruption of Mount St. Helens (Díaz & Rigby, 2022).

The event generated a wide spectrum of atmospheric waves (Matoza et al., 2022) with a salient surface-guided Lamb wave (Francis, 1973) that was detected all around the globe, propagating at ~310 m/s. Carvajal et al. (2022) used globally distributed coastal tide gauge records and found a uniformly small amplitude leading wave moving faster than the expected tsunami. The velocity of the leading wave was very close to the velocity of the atmospheric Lamb wave, as measured by pressure pulses all over the world (Amores et al., 2022; Díaz & Rigby, 2022). Even though the kinetic energy of these waves falls away exponentially from the surface (Vallis, 2017), clear ionospheric perturbations were detected propagating at comparable velocities (~300–320 m/s) (e.g., Lin et al., 2022; Verhulst et al., 2022; Zhang et al., 2022), which suggests that their energy leaked into the thermosphere. Since the neutral density also decreases exponentially with altitude, Lamb waves increase in amplitude with height. The ionospheric disturbances traveled around the world at least three times (Zhang et al., 2022).

The eruption generated regionally localized perturbations as well. In South America, the strongest total electron content (TEC) variations on the day of the event were detected between around 17:00 and 22:00 UT (Takahashi et al., 2023). The onset time of these perturbations approximately coincides with the arrival time of the largest tsunami waves to the western coast of the continent (Carvajal et al., 2022). Additionally, according to

© 2023. The Authors.

This is an open access article under the terms of the [Creative Commons Attribution-NonCommercial-NoDerivs License](https://creativecommons.org/licenses/by-nc-nd/4.0/), which permits use and distribution in any medium, provided the original work is properly cited, the use is non-commercial and no modifications or adaptations are made.

Aa et al. (2022), the American sector presented a notable suppression and deformation of the equatorial ionization anomaly (EIA) crests. The authors reported an EIA reduction of more than 10 total electron content units between 14 and 17 UT, over a 10° latitude range, which was attributed to the passage of the primary Lamb wave.

In this work, we analyze horizontal neutral winds in the mesosphere and lower thermosphere (MLT) associated with the volcanic explosion, calculated using data sets from three multistatic specular meteor radar systems (SMRs) located in South America. The strongest wind variations started around 18 UT on the day of the event, almost simultaneously at the three sites, and lasted for a couple of hours. We start by describing the data sets and the main data analyses in Section 2. The results from customary as well as special analyses of the radar data are presented in Section 3. These results are discussed in Section 4, followed by the conclusions in Section 5.

2. Data Set and Methods

We use three SMRs located near the west coast of the South American continent, in Peru and Chile. These systems are (from North to South): (a) Spread spectrum Interferometric Meteor radar Observing Network (SIMONE) Piura at Universidad de Piura, Peru (5°S, 80°W), (b) SIMONE Jicamarca at the Jicamarca Radio Observatory, Peru (11.9°S, 76.8°W), and (c) Chilean Observation Network De MeteOr Radars (CONDOR) at the Andes lidar Observatory, Chile (30.3°S, 70.7°W). All three systems have multistatic capabilities and therefore allow much more counts than traditional SMRs, and observations of the same volume from different viewing angles. More details of SIMONE Jicamarca and CONDOR, including their operational characteristics, can be found in Conte et al. (2022). SIMONE Piura is similar to SIMONE Jicamarca, but with one additional antenna on transmission and one additional receiver. Specifics of the operational SIMONE systems can be found in Chau et al. (2021).

The products extracted from the systems are the Doppler shift (f_d) for each meteor detection, the measurement errors (ξ), and the Bragg wave vector (scattered minus incident wave vectors; \vec{k}), from which the zonal (east-west; u) and meridional (north-south; v) wind components are calculated, by solving:

$$2\pi f_d = \vec{k} \cdot \vec{u} + \xi. \quad (1)$$

Here, $\vec{u} = (u, v, 0)$ is solved using f_d and \vec{k} of multiple meteor detections with a least-squares approach (Hocking et al., 2001; Holdsworth et al., 2004). Depending on how Equation 1 is solved, the result is \vec{u} distributed in time and altitude bins (Section 3) or in time and horizontal distance bins (Section 3.1). We processed data from 30 December 2021–31 January 2022 but focused on the days near the event (January 15–16). The altitude range explored in this work was 80–100 km.

3. Results

Figure 1 presents the winds as a function of time and altitude for January 15–16. Panels a and b show u and v , respectively; calculated with 1-hr and 2-km time-altitude resolution (u_{1h} and v_{1h}) for CONDOR. The same is shown in panels c and d using 4-hr and 2-km time-altitude resolution (u_{4h} and v_{4h}). Panels e and f show the residuals $u_{res} = u_{1h} - u_{4h}$ and $v_{res} = v_{1h} - v_{4h}$, respectively. The last two rows show residual winds for SIMONE Jicamarca (panels g and h) and for SIMONE Piura (panels i and j), obtained in a similar manner.

The mean wind components $u_{1h}(v_{1h})$ and $u_{4h}(v_{4h})$ show rather typical behavior of mean winds. The meridional component presents a quasi 2-day wave (Q2DW), which is usually strong in this region during January (e.g., Chau et al., 2021; Conte et al., 2021). The Q2DW is also present in the zonal component but with a much smaller amplitude. Below 83 km, the mean zonal wind is mostly westward.

The residual winds of CONDOR allow discerning the high-frequency components. The striking characteristics are two sharp transitions of u_{res} (eastward-to-westward and westward-to-eastward) that occurred around 18:00 UT on January 15. At that moment, u_{res} reached maximum and minimum amplitudes. This behavior was highly coherent in altitude, showing the same characteristics for almost the complete range (80–100 km). While the meridional component also exhibits large $|v_{res}|$ values around the same time, they do not appear to be significantly different from those observed at other times. In fact, there are clear signals with periods of a couple of hours that can be recognized above 88 km during the 2 days shown in the plots.

The residual zonal winds of SIMONE Jicamarca and SIMONE Piura present similar characteristics to CONDOR. The maximum $|u_{res}|$ values occurred around 18:00 UT on January 15. SIMONE Jicamarca also shows large

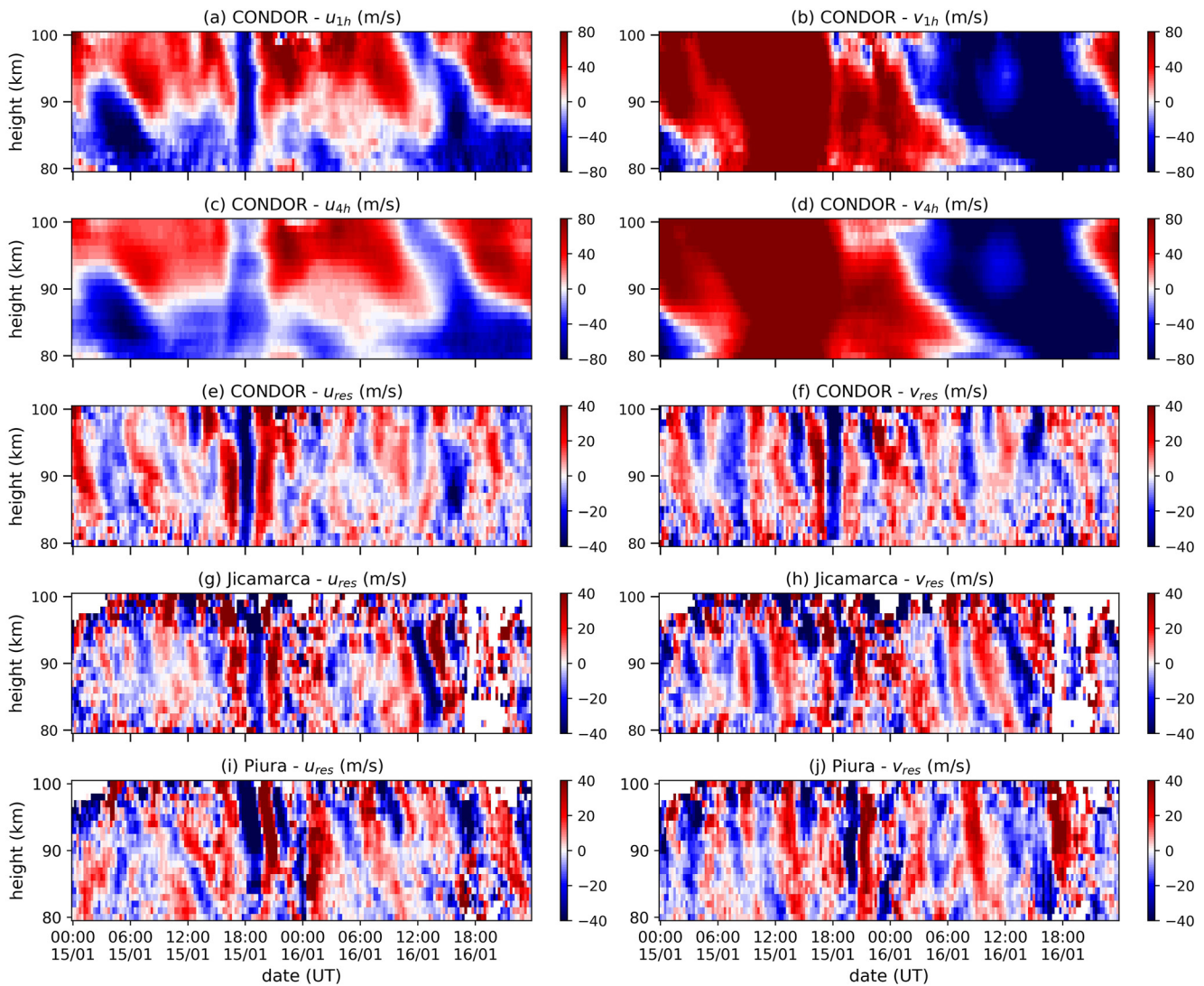


Figure 1. Winds as a function of time and altitude on January 15–16, 2022. Left(right) panels show zonal(meridional) winds for all cases. (a, b): Mean zonal (u_{1h}) and meridional (v_{1h}) winds for CONDOR, calculated using 1-hr and 2-km resolutions. (c, d): Similar to (a, b), using 4 hr and 2 km resolutions (u_{4h} and v_{4h}). (e, f): Residual winds for CONDOR $u_{res} = u_{1h} - u_{4h}$ and $v_{res} = v_{1h} - v_{4h}$. (g, h): u_{res} and v_{res} for SIMONE Jicamarca. (i, j): u_{res} and v_{res} for SIMONE Piura.

amplitudes of u_{res} on January 16 between around 12:00 and 15:00 UT that are not very clear in the residual winds of the other two systems. In all three cases, the negative perturbations reach values smaller than -35 m/s.

To further describe the simultaneous and unusually large wind perturbations on the three systems around 18:00 UT, the residual winds were averaged in altitude. This exploits the consistency of the signal with height, without missing essential details about its period and arrival time. The results for SIMONE Piura, SIMONE Jicamarca, and CONDOR are shown in the first, second, and third rows, respectively, of Figure 2b. The panels on the left(right) correspond to the zonal(meridional) component. The region in gray is bounded by three times the standard deviation (σ) of height-averaged residuals calculated over 33 days around the event. In addition, the map of Figure 2a shows the horizontal distribution of meteor echo reflection points on January 15-16, for the three multistatic SMRs. The gray lines mark the great circles from the epicenter of the event. Note that the meteors from the three locations were detected at similar distances from Tonga.

Given that the height-averaged u_{res} curves exceed $\pm 3\sigma$ around 18:00 UT over the three sites, such perturbation represents an extreme event. It arrives almost simultaneously to the three locations: first to CONDOR at 18:15 UT (shown as a vertical yellow line for reference), then to SIMONE Piura at 18:45 UT, and finally to SIMONE Jicamarca at 19:00 UT. Considering this and the distances shown in the map, it can be inferred that the signal

Multistatic specular meteor radars over west South America

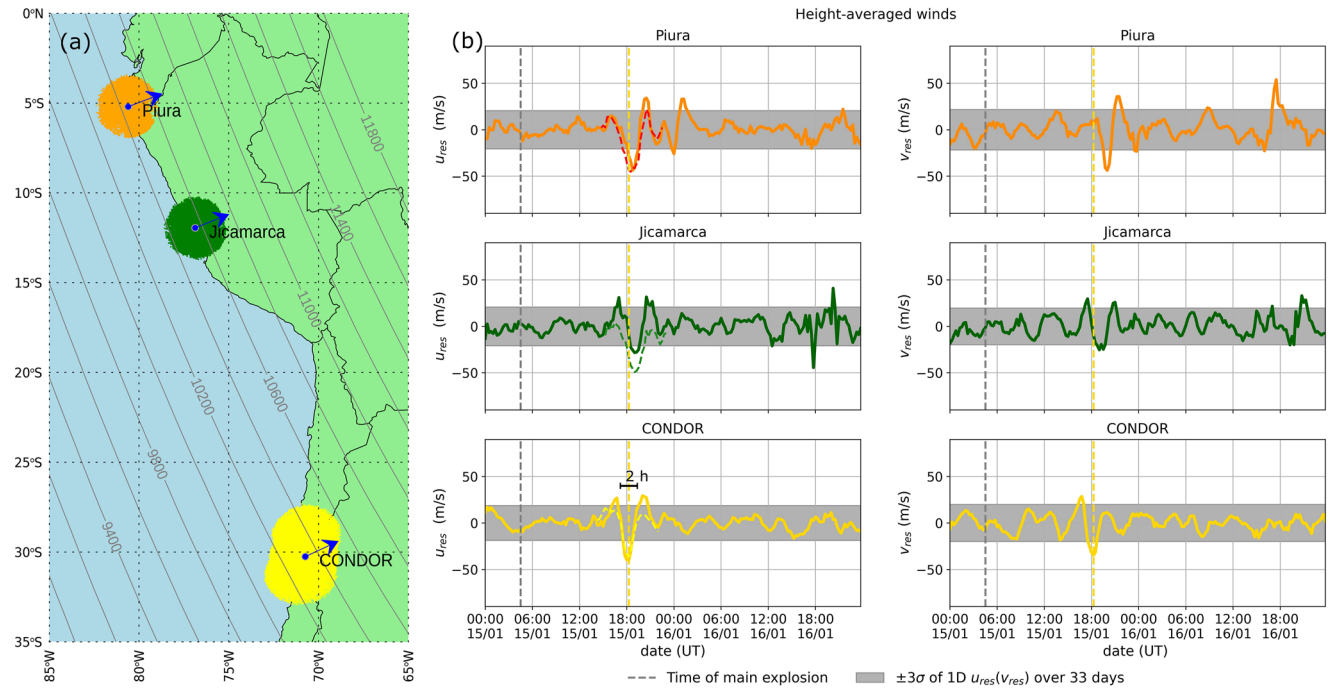


Figure 2. (a) Map of meteor detections of SIMONE Piura (orange), SIMONE Jicamarca (green), and CONDOR (yellow) for January 15–16, 2022. Blue arrows mark the direction of the longitudinal wind component (see text for details), which is perpendicular to the great circles (gray) from the eruption epicenter. (b) Height-averaged zonal (left) and meridional (right) residual winds for the three meteor radar systems. The dashed gray vertical line marks the time of the main explosion (~4:30 UT). The dashed yellow vertical line is aligned with the minimum in CONDOR.

behaves as a radial front moving outwards from the epicenter. Moreover, with the distances and peak times, the average velocity of the front is 205 m/s.

We can draw the same conclusion from the temporal evolution of CONDOR's and SIMONE Jicamarca's height-averaged v_{res} components. However, the SIMONE Piura observations reveal a delay of almost 1 hour in the signal's arrival time compared to the zonal component. This time lag appears to result from local deformations in the propagation front, because they affect only one component at one location. The direction of propagation, which was predominantly eastward, likely amplifies this effect, leading to a clearer pattern on the zonal component, as previously noted in Figure 1.

Next to the signal minimum at ~18 UT, there are clear sidelobes that in most cases also exceed $\pm 3\sigma$. These are most likely a consequence of subtracting $u_{4h}(v_{4h})$ to $u_{1h}(v_{1h})$ in order to derive $u_{res}(v_{res})$ since the sidelobes are not present in $u_{1h}(v_{1h})$ (see Figures 1a and 1b). If we use the zonal component u_{1h} to fit and remove the 48, 24, 12, and 8 hr tidal components (e.g., Conte et al., 2021), we obtain the values shown as dashed lines in the left panels of Figure 2b, which present reduced sidelobes amplitude and slightly larger peak perturbations.

The height-averaged u_{res} curves of SIMONE Jicamarca present high magnitudes on January 16 at ≈ 18 –20 UT, but these are an artifact due to the bad data coverage, as shown by Figure 1g.

3.1. Horizontal Propagation

To complement the analysis of the previous section, we solved for the winds as a function of time and horizontal distance to Tonga, using Equation 1. The vector \vec{u} was calculated in a different decomposition, as $\vec{u} = (u_e, u_t, 0)$ where u_e is the longitudinal component and u_t is the transverse component. To obtain these two components from the inversion problem, each \vec{k} must be rotated at an angle on the horizontal plane, that is delimited by the east-west direction and the direction from Tonga to the position of \vec{k} (Poblet et al., 2023). The result is u_e directed perpendicularly to the great circles shown in Figure 2a, and u_t tangential to them. The direction of u_e is illustrated with blue arrows in Figure 2a.

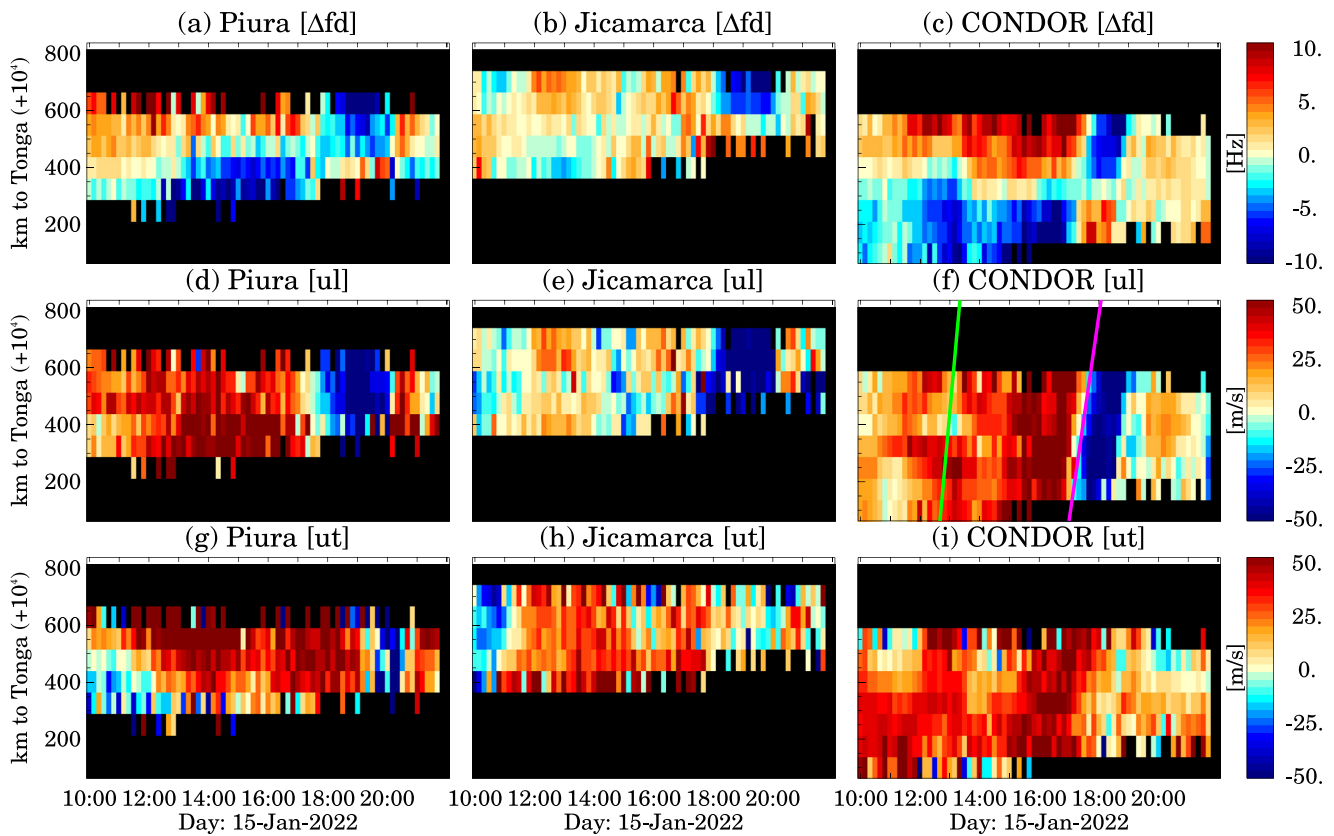


Figure 3. (a–c): Residual Doppler shifts $\Delta f_d = f_d - (\vec{k} \cdot \vec{u}_{4h})/2\pi$ as a function of time and distance to Tonga on January 15. (d–f): Longitudinal velocity components u_ℓ . (g–i): Transverse components u_\perp . The left, center, and right panels show the results for SIMONE Piura, SIMONE Jicamarca, and CONDOR, respectively. Note that 10,000 km must be added to y-axis values to get the proper distance to the epicenter.

Figure 3 shows residual Doppler shifts $\Delta f_d = f_d - (\vec{k} \cdot \vec{u}_{4h})/2\pi$ in the first row, u_ℓ in the second row, and u_\perp in the third row as a function of time and horizontal separation from Tonga. Measurements in the 85–100 km altitude range were combined for this plot. The left, middle, and right columns correspond to SIMONE Piura, SIMONE Jicamarca, and CONDOR, respectively.

Figure 3c shows clear negative-to-positive(positive-to-negative) transitions after 14:00 UT at $\sim 10,350$ km distance. This distance lies approximately at the center of the meteors detection distribution, where the radar network is located. The Doppler shift values over these sites are usually low. Interestingly, this behavior is reflected as positive or negative u_ℓ values (see panel f) for the whole distance range ($\approx 10,200$ – $10,550$ km). For example, u_ℓ in CONDOR shows positive values between around 15:00 and 18:00 UT that turn negative after 18:00 UT until around 19:00 UT. This signal can also be recognized in SIMONE Piura and SIMONE Jicamarca for a wide distance range.

While the longitudinal component exhibits clear wave patterns, the transverse components do not (see Figures 3g–3i). This suggests that the wave-induced motions are parallel to its propagation direction, emphasizing its longitudinal nature. The transverse component in CONDOR exhibits large amplitudes at 15:00–18:00 UT that seem to be also present at SIMONE Piura.

Around 13:00 UT, we have drawn a green line on panel f with a slope corresponding to 310 m/s. These are the expected arrival time to South America and the speed of the L_0 Lamb wave observed in the ionosphere (e.g., Francis, 1973; Zhang et al., 2022). Even though there is a small signal in the CONDOR results, it is not significant enough to be associated with the eruption. The absence of signals related to this wave might be related to the averaging procedure involved to resolve winds from meteor radars. The effect of very high-frequency waves and very fast waves can sometimes be averaged out.

The transition from positive to negative values around 18 UT in Figure 3 along with the assumption that the signal behaves as a wavefront are useful to derive important wave parameters of the perturbation. For example, from the slope of the purple line in Figure 3f, we can estimate a phase velocity of $c_h = 200$ m/s, which correctly fits the wind direction change at multiple distances. This means that the direction of the propagation path did not significantly change throughout the measured MLT volume. This phase speed value is very close to the velocities estimated from Figure 2 in the previous section, using the wind-perturbation peak time and the distances to the epicenter.

From Figure 2b we can infer that the period of the perturbation is $T \simeq 2$ hr. This can be used to approximate the horizontal wavelength as $\lambda_h = Tc_h$, which gives $\lambda_h \simeq 1,440$ km. Here, we are assuming that the background conditions do not significantly affect the propagation of the perturbation. These results are coherent with the ones presented in Figure 1 using the standard vectors decomposition. Namely, given that λ_h is larger than the size of the horizontal meteor-radar coverage area, the traditional analysis averaging structures smaller than ~ 500 km, was able to clearly reproduce the perturbation due to the eruption.

4. Discussion

We described a horizontal wind perturbation that simultaneously reached the MLT volumes captured by the three multistatic SMRs, almost 13.5 hr after Hunga main eruption. Its period was ~ 2 hr with a phase velocity of ~ 200 m/s which allowed us to estimate a horizontal wavelength of around 1,440 km. The signal was notoriously homogeneous with height, suggesting a large vertical wavelength ($\gtrsim 40$ km). Moreover, the observation of the largest TEC perturbations on the continent at ~ 18 UT on January 15 (Takahashi et al., 2023) indicates that the signal may have covered a couple of hundred kilometers in altitude.

The thermosphere (~ 100 – 300 km) exhibited extreme horizontal neutral wind changes (± 200 m/s) on the day of the event, at a distance of 9,000–14,000 km from the volcano's epicenter, which lasted for at least 6–7 hr (Aa et al., 2022; Harding et al., 2022). These wind variations were detected by satellite observations, which map wide altitude and longitude intervals with relatively coarse resolutions when compared to SMR measurements. The radars observe only the lowermost part of the altitude range covered by the satellite. In addition, another factor that renders the comparison between the ~ 18 UT MLT perturbation in South America and the extreme wind changes observed by the satellite intricate is that we have analyzed residual winds, which are fluctuations superimposed on the mean wind, whereas Aa et al. (2022) and Harding et al. (2022) reported measurements of the total wind, where the mean wind dominates the dynamics.

The nature of the perturbation is a subject of debate, as it is unclear whether it is solely an atmospheric phenomenon or if an air-to-sea coupling mechanism caused it. This dilemma is heightened by the fact that the largest tsunami waves resulting from the eruption arrived on the continent at the same time (Carvajal et al., 2022).

The simulations by Liu et al. (2023) support the atmospheric phenomenon hypothesis. The authors used the Whole Atmosphere Community Climate Model with thermosphere/ionosphere extension (WACCM-X) to reproduce the event, simulating Lamb waves with increasing temperature and wind amplitudes with altitude. The results indicated that a 100-km altitude L_1 Lamb-wave mode reached the west coast of South America around 18 UT and could be a credible explanation for our observations. This mode's phase and group velocities are slower than the primary L_0 mode and accelerate with the wave period (Francis, 1975). The Lamb wave modes are ducted-mode solutions to the dispersion relation of realistic atmospheres. They were first discovered in attempts to understand the atmospheric response to large volcanic eruptions or nuclear explosions (Francis, 1973; Pfeffer & Zariachny, 1962; Yamamoto, 1957) such as Hunga's 2022 event. Even though the L_1 mode is a non-perfectly ducted mode for large enough periods, it can travel tens of thousands of kilometers before it dissipates. In addition, unlike the L_0 mode that has maximum kinetic energy values at the surface, the L_1 mode reaches its peak in the mesosphere (see Francis, 1973, figure 11). Note that the phase speed values reported by Francis (1973) are a bit larger (250–260 m/s) than the one estimated in this work. The deviations can arise from the modeling side, by assuming parameter values that differ from the real ones, for example, the vertical profile of kinematic viscosity, the background density and temperature. But they can also come from the observation side, for example, by local deformations of the propagation front that can make it difficult to accurately fit phase velocities.

On the other hand, the signal could be interpreted as an effect of the Tsunami triggered by the eruption. Vadas et al. (2015) modeled the gravity waves (GWs) excited by an ocean surface wave packet (localized in space

and time), represented as a vertical body force. They found that ocean wave packets with large enough periods generate continuum GWs in the thermosphere with much faster horizontal phase velocities than that of the ocean wave. Then, they can reach distant positions faster than the ocean wave packet. This is in agreement with Hunga's 2022 event since the arrival of the largest Tsunami waves to the coasts of South America occurred one or two hours after the ~ 18 UT signal in the MLT and the ionosphere (see Carvajal et al., 2022, figure 3 and supplementary files). Something similar was reported by Makela et al. (2011), who encountered early GWs in the 630 nm airglow layer approximately 1 hr before the Tohoku tsunami reached Hawaii.

However, one aspect of our observations is not compatible with the main result in Vadas et al. (2015). The localized body force proposed in the model excites a spectrum of GWs that contains particular frequencies as well as a continuum of frequencies, thus resulting in GWs with varied phase speeds. On the contrary, the ~ 18 UT MLT signal does not display this polychromatic fashion in any of the three locations.

5. Conclusions

By combining three well-separated multistatic SMR stations almost aligned with a propagation front originated by the 2022 Hunga eruption, we have been able to clearly identify an elongated wavefront in the MLT with extreme wind perturbations over the western part of South America. Considering its observed and derived parameters, this wave is a Lamb wave but propagating at a relatively slow velocity of ~ 200 m/s at the observation time. WACCM-X simulations indicate that the wave is a so-called L_1 -mode Lamb wave. However, we are not in a position to rule out a possible connection to the tsunami that arrived at a similar time to the western South American coast after the eruption. Other perturbations associated with the eruption appear to be present in our data but given their relatively weak amplitudes, and their absence in one or two of the stations, their clear characterization has not been possible. Finally, we are curious to determine the precise extent of the wavefront that propagated the perturbation. To do this, we could examine data gathered by other ground-based radars and apply some of the customized analysis techniques utilized in this study.

Data Availability Statement

The SMR data products used in this work can be found in Poblet (2023).

References

- Aa, E., Zhang, S.-R., Wang, W., Erickson, P. J., Qian, L., Eastes, R., et al. (2022). Pronounced suppression and x-pattern merging of equatorial ionization anomalies after the 2022 Tonga volcano eruption. *Journal of Geophysical Research: Space Physics*, 127(6), e2022JA030527. <https://doi.org/10.1029/2022JA030527>
- Amores, A., Monserrat, S., Marcos, M., Argüeso, D., Villalonga, J., Jordà, G., & Gomis, D. (2022). Numerical simulation of atmospheric lamb waves generated by the 2022 Hunga-Tonga volcanic eruption. *Geophysical Research Letters*, 49(6), e2022GL098240. <https://doi.org/10.1029/2022GL098240>
- Carvajal, M., Sepúlveda, I., Gubler, A., & Garreaud, R. (2022). Worldwide signature of the 2022 Tonga volcanic tsunami. *Geophysical Research Letters*, 49(6), e2022GL098153. <https://doi.org/10.1029/2022GL098153>
- Chau, J. L., Urco, J. M., Vierinen, J., Harding, B. J., Clahsen, M., Pfeffer, N., et al. (2021). Multistatic specular meteor radar network in Peru: System description and initial results. *Earth and Space Science*, 8(1), e2020EA001293. <https://doi.org/10.1029/2020ea001293>
- Conte, J. F., Chau, J. L., Liu, A., Qiao, Z., Fritts, D. C., Hormaechea, J. L., et al. (2022). Comparison of MLT momentum fluxes over the Andes at four different latitudinal sectors using multistatic radar configurations. *Journal of Geophysical Research: Atmospheres*, 127(4), e2021JD035982. <https://doi.org/10.1029/2021JD035982>
- Conte, J. F., Chau, J. L., Urco, J. M., Latteck, R., Vierinen, J., & Salvador, J. O. (2021). First studies of mesosphere and lower thermosphere dynamics using a multistatic specular meteor radar network over southern Patagonia. *Earth and Space Science*, 8(2), e2020EA001356. <https://doi.org/10.1029/2020ea001356>
- Díaz, J. S., & Rigby, S. E. (2022). Energetic output of the 2022 Hunga Tonga–Hunga Ha’apai volcanic eruption from pressure measurements. *Shock Waves*, 32(6), 553–561. <https://doi.org/10.1007/s00193-022-01092-4>
- Francis, S. H. (1973). Acoustic-gravity modes and large-scale traveling ionospheric disturbances of a realistic, dissipative atmosphere. *Journal of Geophysical Research*, 78(13), 2278–2301. <https://doi.org/10.1029/ja078i013p02278>
- Francis, S. H. (1975). Global propagation of atmospheric gravity waves: A review. *Journal of Atmospheric and Terrestrial Physics*, 37(6–7), 1011–1054. [https://doi.org/10.1016/0021-9169\(75\)90012-4](https://doi.org/10.1016/0021-9169(75)90012-4)
- Global Volcanism Program. (2022). Report on Hunga Tonga–Hunga Ha’apai (Tonga)—February 2022. *Bulletin of the Global Volcanism Network*, 47(2). <https://doi.org/10.5479/si.gvp.bgvn202202-243040>
- Harding, B. J., Wu, Y.-J. J., Alken, P., Yamazaki, Y., Triplett, C. C., Immel, T. J., et al. (2022). Impacts of the January 2022 Tonga volcanic eruption on the ionospheric dynamo: Ion-mighti and swarm observations of extreme neutral winds and currents. *Geophysical Research Letters*, 49(9), e2022GL098577. <https://doi.org/10.1029/2022GL098577>
- Hocking, W., Fuller, B., & Vandeppeer, B. (2001). Real-time determination of meteor-related parameters utilizing modern digital technology. *Journal of Atmospheric and Solar-Terrestrial Physics*, 63(2–3), 155–169. [https://doi.org/10.1016/s1364-6826\(00\)00138-3](https://doi.org/10.1016/s1364-6826(00)00138-3)

Acknowledgments

We thank Hanli Liu for suggesting the hypothesis of the L_1 Lamb-wave mode to explain the signal described in this work and for valuable comments on the elaboration of this manuscript. We also thank Karim Kuyeng, the staff of the Jicamarca Radio Observatory, and the Estación Científica Ramon Mugica of the Universidad de Piura (UDEP) in Peru for operating and maintaining the SIMONe Jicamarca and SIMONe Piura systems. This work was partially financed by the Leibniz SAW project FORMOSA (Grant K227/2019). Open Access funding enabled and organized by Projekt DEAL.

- Holdsworth, D. A., Reid, I. M., & Cervera, M. A. (2004). Buckland park all-sky interferometric meteor radar. *Radio Science*, 39(5). <https://doi.org/10.1029/2003rs003014>
- Lin, J.-T., Rajesh, P. K., Lin, C. C., Chou, M.-Y., Liu, J.-Y., Yue, J., et al. (2022). Rapid conjugate appearance of the giant ionospheric lamb wave signatures in the northern hemisphere after Hunga-Tonga volcano eruptions. *Geophysical Research Letters*, 49(8), e2022GL098222. <https://doi.org/10.1029/2022gl098222>
- Liu, H., Wang, W., Huba, J. D., Lauritzen, P. H., & Vitt, F. (2023). Atmospheric and ionospheric responses to Hunga-Tonga volcano eruption simulated by WACCM-X. *Geophysical Research Letters*, e2023GL103682. <https://doi.org/10.1029/2023GL103682>
- Makela, J., Lognonné, P., Hébert, H., Gehrels, T., Rolland, L., Allgeyer, S., et al. (2011). Imaging and modeling the ionospheric airglow response over Hawaii to the tsunami generated by the Tohoku earthquake of 11 March 2011. *Geophysical Research Letters*, 38(24). <https://doi.org/10.1029/2011gl047860>
- Matoza, R. S., Fee, D., Assink, J. D., Iezzi, A. M., Green, D. N., Kim, K., et al. (2022). Atmospheric waves and global seismoacoustic observations of the January 2022 Hunga eruption, Tonga. *Science*, 377(6601), 95–100. <https://doi.org/10.1126/science.abo7063>
- Pfeffer, R. L., & Zarichny, J. (1962). Acoustic-gravity wave propagation from nuclear explosions in the Earth's atmosphere. *Journal of the Atmospheric Sciences*, 19(3), 256–263. [https://doi.org/10.1175/1520-0469\(1962\)019<0256:agwpfn>2.0.co;2](https://doi.org/10.1175/1520-0469(1962)019<0256:agwpfn>2.0.co;2)
- Poblet, F. L. (2023). Data files - PobletGRL2023. RADAR — Research data repository. <https://doi.org/10.22000/956>
- Poblet, F. L., Vierinen, J., Avsarkisov, V., Conte, J. F., Asokan, H. C., Jacobi, C., & Chau, J. L. (2023). Horizontal correlation functions of wind fluctuations in the mesosphere and lower thermosphere. *Journal of Geophysical Research: Atmospheres*, 128(6), e2022JD038092. <https://doi.org/10.1029/2022JD038092>
- Takahashi, H., Figueiredo, C., Barros, D., Wrasse, C., Giongo, G., Honda, R., et al. (2023). Ionospheric disturbances over South America related to Tonga volcanic eruption. *Earth Planets and Space*, 75(1), 92. <https://doi.org/10.1186/s40623-023-01844-1>
- Vadas, S. L., Makela, J. J., Nicolls, M. J., & Milliff, R. F. (2015). Excitation of gravity waves by ocean surface wave packets: Upward propagation and reconstruction of the thermospheric gravity wave field. *Journal of Geophysical Research: Space Physics*, 120(11), 9748–9780. <https://doi.org/10.1002/2015ja021430>
- Vallis, G. K. (2017). Gravity waves. In *Atmospheric and oceanic fluid dynamics: Fundamentals and large-scale circulation* (2nd ed., pp. 251–296). Cambridge University Press. <https://doi.org/10.1017/9781107588417.008>
- Verhulst, T. G., Altadill, D., Barta, V., Belehaki, A., Burešová, D., Cesaroni, C., et al. (2022). Multi-instrument detection in Europe of ionospheric disturbances caused by the 15 January 2022 eruption of the Hunga volcano. *Journal of Space Weather and Space Climate*, 12, 35. <https://doi.org/10.1051/swsc/2022032>
- Yamamoto, R. (1957). A dynamical theory of the microbarographic oscillations produced by the explosions of hydrogen bombs. *Journal of the Meteorological Society of Japan. Series II*, 35(5), 288–296. https://doi.org/10.2151/jmsj1923.35.5_288
- Zhang, S.-R., Vierinen, J., Aa, E., Goncharenko, L. P., Erickson, P. J., Rideout, W., et al. (2022). 2022 Tonga volcanic eruption induced global propagation of ionospheric disturbances via Lamb waves. *Frontiers in Astronomy and Space Sciences*, 9. <https://doi.org/10.3389/fspas.2022.871275>